

1  
2  
3 **Gold Nanoparticle Plasmonic Superlattices as Surface Enhanced Raman**  
4  
5 **Spectroscopy Substrates**  
6  
7

8  
9 *Cristiano Matricardi,<sup>1,&</sup> Christoph Hanske,<sup>2,&</sup> Juan Luis Garcia-Pomar,<sup>1</sup> Judith*  
10  
11 *Langer,<sup>2</sup> Agustín Mihi,<sup>1,\*</sup> and Luis M. Liz-Marzán<sup>2,3,\*</sup>*  
12  
13

14 <sup>1</sup>Institut de Ciència de Materials de Barcelona (ICMAB-CSIC), Campus de la  
15 UAB, 08193 Bellaterra, Catalonia, Spain

16 <sup>2</sup>CIC biomaGUNE and Ciber-BBN, Paseo de Miramón 182, 20014 Donostia –  
17 San Sebastián, Spain

18 <sup>3</sup>Ikerbasque, Basque Foundation for Science, 48013 Bilbao, Spain  
19

20  
21 *&These authors contributed equally to this work*

22 *(\*corresponding authors: [amihi@icmab.es](mailto:amihi@icmab.es) and [llizmarzan@cicbiomagune.es](mailto:llizmarzan@cicbiomagune.es))*  
23  
24  
25

26 **KEYWORDS:** *SERS, gold nanoparticles, lattice plasmon, self-assembly, Rayleigh*  
27  
28 *anomaly*  
29

30  
31 **Abstract**  
32  
33

34 Metal colloids are of great interest in the field of nanophotonics, mainly due to their  
35 morphology-dependent optical properties, but also because they are high quality  
36 building blocks for complex plasmonic architectures. Close-packed colloidal  
37 supercrystals not only serve for investigating the rich plasmonic resonances arising in  
38 strongly coupled arrangements, but also enables tailoring the optical response, on both  
39 the nano- and the macroscale. Bridging these vastly different length scales at reasonable  
40 fabrication costs has remained fundamentally challenging, but is essential for  
41 applications in sensing, photovoltaics or optoelectronics, among other fields. We  
42 present here a scalable approach to engineer plasmonic supercrystal arrays, based on the  
43 template-assisted assembly of gold nanospheres with topographically patterned  
44 polydimethylsiloxane molds. Regular square arrays of hexagonally packed supercrystals  
45  
46  
47  
48  
49  
50  
51  
52  
53  
54  
55  
56  
57  
58  
59  
60

1  
2  
3 were achieved, reaching periodicities down to 400 nm and feature sizes around 200 nm,  
4  
5 over areas up to 0.5 cm<sup>2</sup>. These two-dimensional supercrystals exhibit well-defined  
6  
7 collective plasmon modes that can be tuned from the visible through the near-infrared  
8  
9 by simple variation of the lattice parameter. We present electromagnetic modelling of  
10  
11 the physical origin of the underlying hybrid modes, and demonstrate the application of  
12  
13 superlattice arrays as surface-enhanced Raman scattering (SERS) spectroscopy  
14  
15 substrates which can be tailored for a specific probe laser. We therefore investigated the  
16  
17 influence of the lattice parameter, local degree of order, and cluster architecture, to  
18  
19 identify the optimal configuration for highly efficient SERS of a non-resonant Raman  
20  
21 probe with 785 nm excitation.  
22  
23  
24  
25

26  
27 Ultrasensitive molecular detection and specific quantification of analytes have been  
28  
29 leading motivations in the development of advanced spectroscopic techniques.<sup>1</sup> Raman  
30  
31 spectroscopy, which probes vibrational transitions, allows the label-free identification of  
32  
33 a wide variety of molecules, thereby becoming a highly relevant tool in disciplines  
34  
35 including biology, medicine, or forensics.<sup>2-4</sup> However, the extremely low cross section  
36  
37 of Raman scattering usually requires either large amounts of analyte or very powerful  
38  
39 laser sources, which can in turn degrade the molecules.<sup>5</sup> Surface-enhanced Raman  
40  
41 scattering (SERS) has mitigated this issue, on the basis of the amplification of the  
42  
43 Raman signal of molecules in contact with nanostructured metallic surfaces.<sup>6,7</sup> The main  
44  
45 mechanism behind the observed huge Raman signals is the electromagnetic  
46  
47 enhancement, due to a local confinement of the electromagnetic field, which is  
48  
49 especially strong within plasmonic hot spots between close-packed metal  
50  
51 nanoparticles.<sup>8</sup>  
52  
53  
54  
55  
56  
57  
58  
59  
60

1  
2  
3 Consequently, colloidal mesostructures have a great potential as highly effective SERS  
4 substrates,<sup>9,10</sup> whereby their performance depends sensitively on the interparticle  
5 distance.<sup>11,12</sup> Direct writing techniques like e-beam or focused ion beam lithography  
6  
7 can be used to obtain nanoparticle arrangements with the nanometer-sized gaps  
8  
9 necessary for SERS, but are very inefficient in terms of time and cost.<sup>13</sup> Therefore, self-  
10  
11 assembly of chemically synthesized plasmonic nanoparticles is often utilized for  
12  
13 substrate preparation. Methods as simple as drop casting or precipitation of colloidal  
14  
15 dispersions may yield assemblies that are able to sufficiently amplify Raman cross  
16  
17 sections and enable even single molecule detection,<sup>14-16</sup> which however usually comes  
18  
19 at the cost of poor signal reproducibility.<sup>17,18</sup> Strategies for preparing homogeneously  
20  
21 structured nanoparticle films by template-assisted self-assembly have been improved  
22  
23 significantly over the last decade, now having the potential to solve the above  
24  
25 mentioned issues.<sup>19-22</sup> These substrates featuring both a high density of hot spots and  
26  
27 improved uniformity have been employed, for example, in the detection of gases like  
28  
29 carbon monoxide or pyrene,<sup>23,24</sup> as well as in monitoring the expression of bacterial  
30  
31 quorum sensing molecules *via* SERS.<sup>25</sup>  
32  
33  
34  
35  
36  
37

38 The occurrence of collective plasmon resonances is directly connected to the presence  
39  
40 of hot spots in metal nanoparticle assemblies, which often dominate the optical response  
41  
42 of nanoparticle films.<sup>26-28</sup> Near-field coupling between neighboring NPs can give rise to  
43  
44 hybridized modes in clusters. These resonances are usually red-shifted and broadened  
45  
46 compared to the localized surface plasmon resonances (LSPRs) of isolated particles.  
47  
48 Besides single particle properties and gap size, the frequencies at which such collective  
49  
50 resonances appear, depend on cluster size and symmetry.<sup>22,29</sup> Further, the introduction  
51  
52 of superordinate periodic patterns can give rise to additional diffractive resonances due  
53  
54 to optical far-field interactions. These so-called lattice plasmon modes can be tuned  
55  
56  
57  
58  
59  
60

1  
2  
3 over a wide frequency range by varying lattice parameters and have been reported to  
4 yield remarkably sharp resonances.<sup>21,28,30</sup> Intriguingly, Reinhard *et al.* were able to  
5 demonstrate within micrometer-sized areas, the effect of the e-field enhancement of  
6 periodic nanoparticle cluster arrays on the intensity of the SERS signal.<sup>31,32</sup> Taking into  
7 account the manifold factors determining the overall field enhancement in these  
8 assemblies, such as cluster dimensions, lattice parameters, number of layers, and the  
9 overall degree of order, a detailed investigation is required to fully understand and  
10 utilize the complex electromagnetic coupling modes within and between clusters. The  
11 ability of tuning the frequency of these hybrid plasmonic-photonic resonances further  
12 facilitates nanophotonic device engineering.<sup>33</sup> Still, the challenge resides in fabricating  
13 hierarchical assemblies that operate at visible wavelengths and display sufficiently good  
14 homogeneity over macroscopic areas.<sup>34,35</sup>

15  
16  
17  
18  
19  
20  
21  
22  
23  
24  
25  
26  
27  
28  
29 We present in this work a scalable, template-assisted assembly technique, capable of  
30 arranging gold nanospheres (AuNSs) into regular, periodic arrays of well-defined  
31 plasmonic clusters over large areas. The obtained 2D superlattices exhibit both strong  
32 near-field coupling and an optical response that can be tuned from the visible through  
33 the near-infrared (NIR). Topographically patterned elastomeric molds featuring square  
34 arrays of submicrometer-sized holes were used to guide the assembly of monodisperse  
35 AuNSs into organized cluster arrays, over areas up to 0.5 cm<sup>2</sup>. The specific pattern on  
36 the polydimethylsiloxane (PDMS) mold determines the cluster diameter and lattice  
37 parameter, whereas the concentration of the AuNSs dispersion determines the number  
38 of particle layers in the clusters and the overall quality of the assembly. The distinct  
39 plasmonic-photonic hybrid resonances recorded by microspectroscopy can be precisely  
40 reproduced and explained by numerical simulations. These results allow us to tailor the  
41 optical response of the substrates for excitation with specific or available laser lines. In  
42  
43  
44  
45  
46  
47  
48  
49  
50  
51  
52  
53  
54  
55  
56  
57  
58  
59  
60

1  
2  
3 addition, we studied the correlation between the plasmon resonances sustained by the  
4  
5 different geometrical assemblies and their performance as SERS substrates under 785  
6  
7 nm excitation of the Raman probe 4-acetamidothiophenol (4-AMTP). This laser line fits  
8  
9 the first biological optical transparency window, thus providing enhanced light  
10  
11 penetration in tissues, and is particularly interesting for biomolecular detection in  
12  
13 complex media.  
14  
15  
16  
17  
18

## 19 **Results and Discussion**

20  
21  
22 The monodisperse gold nanoparticles used in this work were stabilized with (PEG, 6kD)  
23  
24 and featured an average diameter of 52 nm (standard deviation: 2 nm), with a  
25  
26 corresponding LSPR at  $\lambda_{LSPR} = 532$  nm (**Figure S1, SI**). The use of patterned PDMS  
27  
28 molds to fabricate nanopatterned SERS substrates,<sup>36</sup> or to direct the assembly of gold  
29  
30 colloids into ordered arrays, is an appealing approach due to both the intrinsic low cost  
31  
32 of the technique and the large areas that can be attained. Successful template-assisted  
33  
34 self-assembly of AuNSs has been previously reported into micrometer-sized square  
35  
36 pyramids,<sup>37</sup> leading to highly regular plasmonic supercrystals. This was, however,  
37  
38 unsuitable to obtain structures exhibiting a strong optical response at visible  
39  
40 wavelengths, for which the cluster arrays should feature order at the submicrometer  
41  
42 scale.<sup>31</sup> Such a structuration was achieved in the present work, by using PDMS molds  
43  
44 featuring square array geometries with lattice parameters ( $L$ ) of 400, 500, 600, 740 and  
45  
46 1600 nm, and hole diameters ( $d$ ) of 230, 270, 330, 440 and 960 nm, respectively (see  
47  
48  
49  
50 **Methods**).  
51  
52  
53  
54  
55  
56  
57  
58  
59  
60

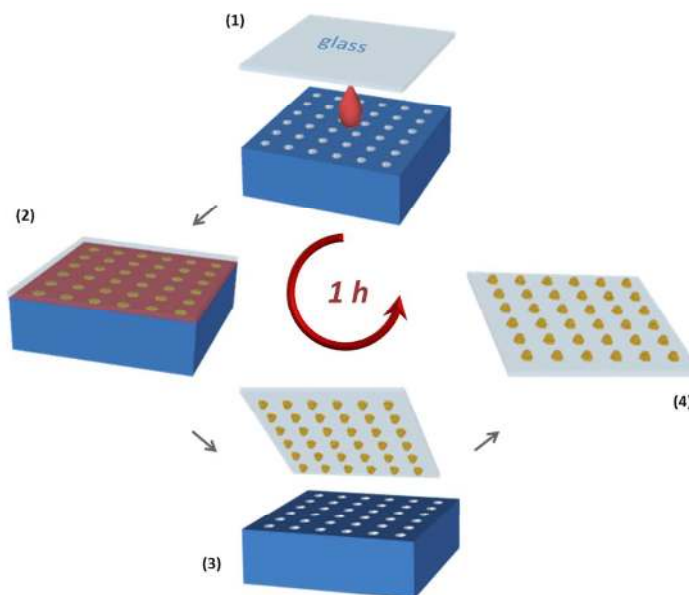
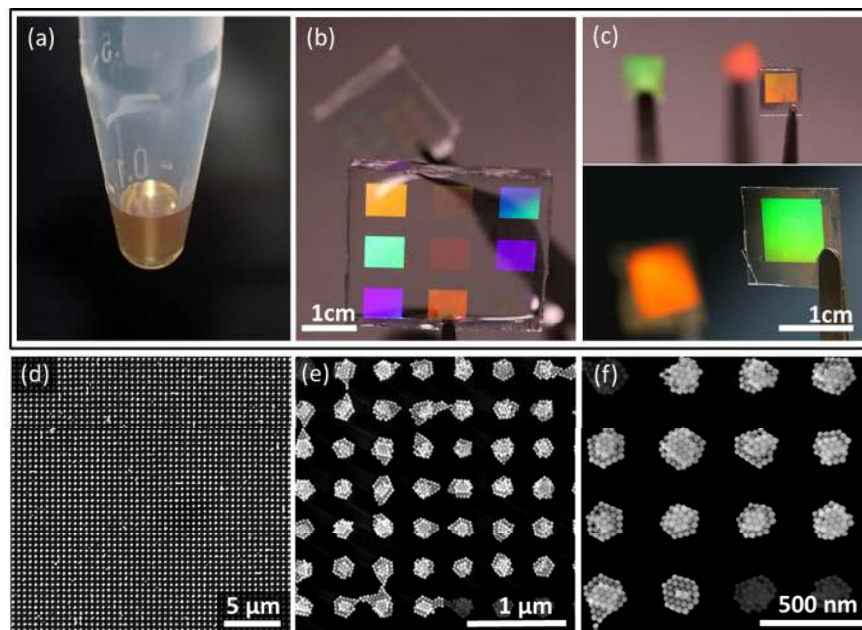


**Figure 1.** Schematic representation of the template-assisted assembly of gold nanospheres into hierarchical superlattices: (1) Deposition of an aqueous AuNSs dispersion on the surface of a patterned PDMS stamp. (2) A glass coverslip is placed on top of the PDMS, spreading the colloidal dispersion over the patterned surface. (3) Removal of the glass substrate carrying the assembled superlattice.

The process of template-assisted assembly of AuNSs into arrays of close-packed, mesoscopic clusters is depicted in **Figure 1**. First, a drop (1  $\mu\text{L}$ ) of the AuNS colloidal dispersion (**Figure 2a**) is deposited on the surface of a PDMS mold (**Figure 2b**) patterned with square arrays of holes, with  $L$  ranging from 400 to 1600 nm and similar filling factors. The filling factor ( $FF$ ), corresponds to the percentage of effective area that can be covered with nanoparticles and is defined as  $FF = \frac{\pi R^2}{L^2}$ , with  $R$  being the radius of the holes, which yields  $FF \sim 0.25 - 0.27$  for the employed stamp geometries. Second, a hydrophilized glass coverslip is placed on top of the PDMS surface, spreading the colloid into the PDMS features that direct the assembly. Finally, after about 1 hour, evaporation of the dispersion medium (water) is completed and the glass substrate carrying the assembled AuNSs can be carefully lifted off. The supercrystal films (**Figure 2c**) display iridescent colors under white light illumination, showing an

1  
2  
3 angular dependence similar to that of the corresponding molds. Scanning electron  
4 microscopy (SEM) images (**Figure 2 d-f**) from representative samples evidence the  
5 long-range order of the AuNS clusters on glass. It is worth noting that the AuNSs pack  
6 hexagonally within the clusters, and that even for a fixed hole size the width and height  
7 of individual assemblies can vary slightly.  
8  
9  
10  
11  
12



13  
14  
15  
16  
17  
18  
19  
20  
21  
22  
23  
24  
25  
26  
27  
28  
29  
30  
31  
32  
33  
34  
35  
36 **Figure 2.** Upper panel: Photographs of a dispersion of AuNSs (a), the PDMS molds  
37 used for the assembly (b), and AuNS assemblies obtained on glass (c). Lower panel:  
38 SEM micrographs of representative square lattice AuNS clusters, at different  
39 magnifications (d-f).  
40

41  
42  
43 The efficiency of AuNS assemblies for sensing is largely determined by their optical  
44 response. Therefore, we optimized the templated assembly conditions, guided by optical  
45 measurements (extinction=1-R-T, where R and T correspond to Reflectance and  
46 Transmittance spectra from the films) and SEM inspection. We thus prepared  
47 assemblies with varying AuNS concentrations (see **Figure S2, SI**), concluding that the  
48 average number of particles per cluster could be adjusted *via* the AuNS concentration  
49 and had a pronounced influence on the optical quality of the substrates. Combined  
50  
51  
52  
53  
54  
55  
56  
57  
58  
59  
60

1  
2  
3 inspection of the topology and the extinction spectra indicated that ordered assemblies  
4 with well-defined plasmon resonances were obtained for intermediate Au  
5 concentrations (33 - 40 mM). Lower concentrations resulted in incomplete clusters with  
6 broad resonances, whereas higher concentrations produced accumulation or bridging  
7 with additional AuNSs between clusters, accompanied by an increased optical  
8 background.  
9  
10

11  
12  
13  
14  
15  
16 The influence of the array periodicity on the optical response was studied using  
17 assemblies with lattice parameters ranging from 400 to 1600 nm, made from dispersions  
18 with optimized gold concentration. Representative SEM images and extinction spectra  
19 of the resulting cluster arrays are displayed in **Figure 3**. From inspection of the optical  
20 spectra, two main regions can be identified: the first region at lower wavelengths shows  
21 a local extinction maximum at  $\lambda \sim 560$  nm. This peak is close to the dipolar mode of a  
22 single AuNS ( $\lambda_{LSPR} = 532$  nm in water) and is likely influenced by higher order  
23 coupling modes of the clusters, which are typically observed for interparticle distances  
24 smaller than 2 nm.<sup>28,38</sup> When the NSs within the clusters are closer to each other, a  
25 stronger degree of plasmon coupling can be expected, and higher order cluster modes  
26 appear at energies close to the single particle LSPR. These higher order cluster modes,  
27 which have been discussed in previous works,<sup>28,38</sup> can shift the peak to  $\lambda \sim 560$  nm.<sup>22,39</sup>  
28  
29  
30  
31  
32  
33  
34  
35  
36  
37  
38  
39  
40  
41  
42  
43  
44  
45  
46  
47  
48  
49  
50  
51  
52  
53  
54  
55  
56  
57  
58  
59  
60

The second region at higher wavelengths displays the most intense extinction peak and clearly red-shifts when increasing the lattice parameter of the assembly. The strong correlation of the latter extinction peak with the lattice parameter indicates that this resonance originates from the hybridization of the plasmonic cluster modes with the diffractive lattice mode.



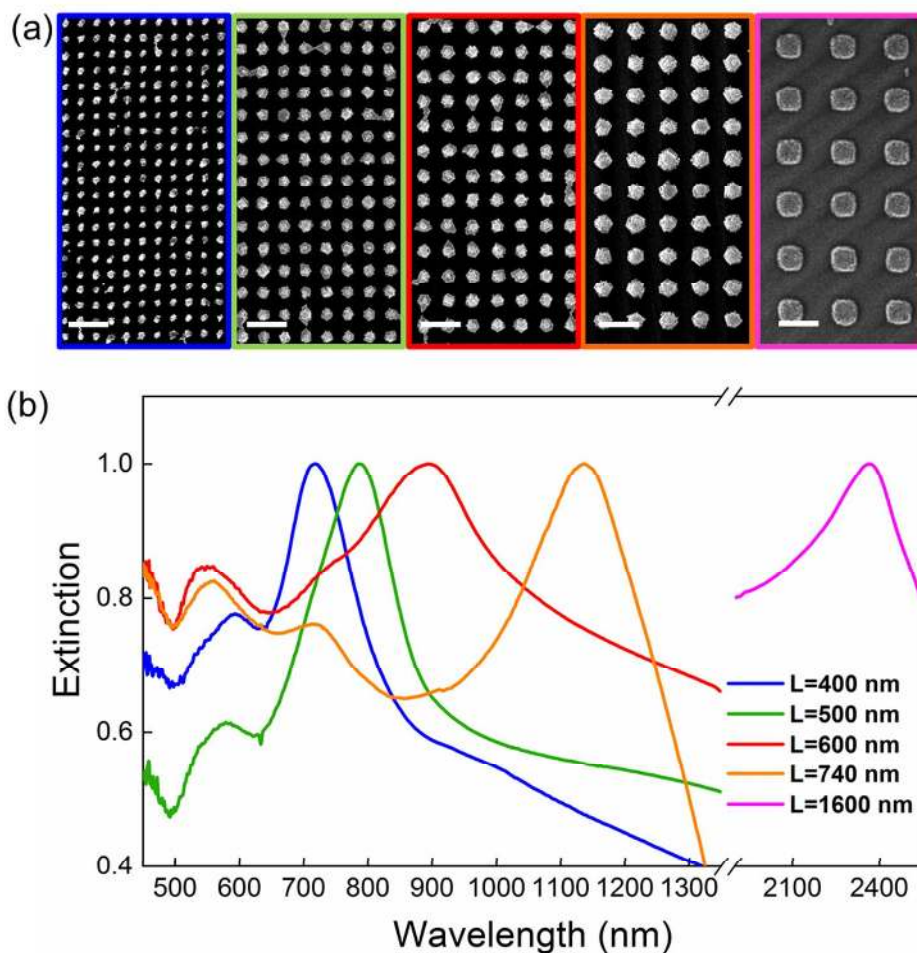


**Figure 3.** Structural and optical characterization of supercrystal assemblies with varying lattice parameter  $L$ . (a) SEM micrographs of gold nanoparticle arrays with different lattice parameters: from left to right  $L=400$  nm,  $L=500$  nm,  $L=600$  nm,  $L=740$  nm, and  $L=1600$  nm. (b) Extinction spectra, normalized to the maximum, of AuNS cluster arrays with different lattice parameters (see labels). Scale bar: 1  $\mu$ m.

These resonances, launched by light diffracted by the grating, are typically called surface lattice resonances,<sup>40</sup> and are usually observed near a Rayleigh anomaly, *i.e.*, a change in the magnitude of the reflectivity associated with the onset of diffraction from the grating.<sup>41</sup> Rayleigh anomalies are grazing waves propagating in the plane of the array. In our system, the electromagnetic field tends to concentrate in the regions with the highest refractive index. As a consequence, the light scattered at the Rayleigh anomaly propagates at the glass, and hybridization of the collective surface plasmon

resonances inside the AuNS clusters with the lattice modes is dominated by the refractive index of the substrate (**Figure S4**).<sup>42,43</sup> This implies that the wavelength position of the lattice modes can be predicted *via* a simple formula, corresponding to the first order of diffraction,  $\lambda_{max} \approx Ln_{glass}$ , where  $n_{glass}$  is the refractive index of the glass substrate. This formula fits very accurately with the positions of the maxima observed for different lattice parameters  $L$ , as shown in **Figure 3b**.

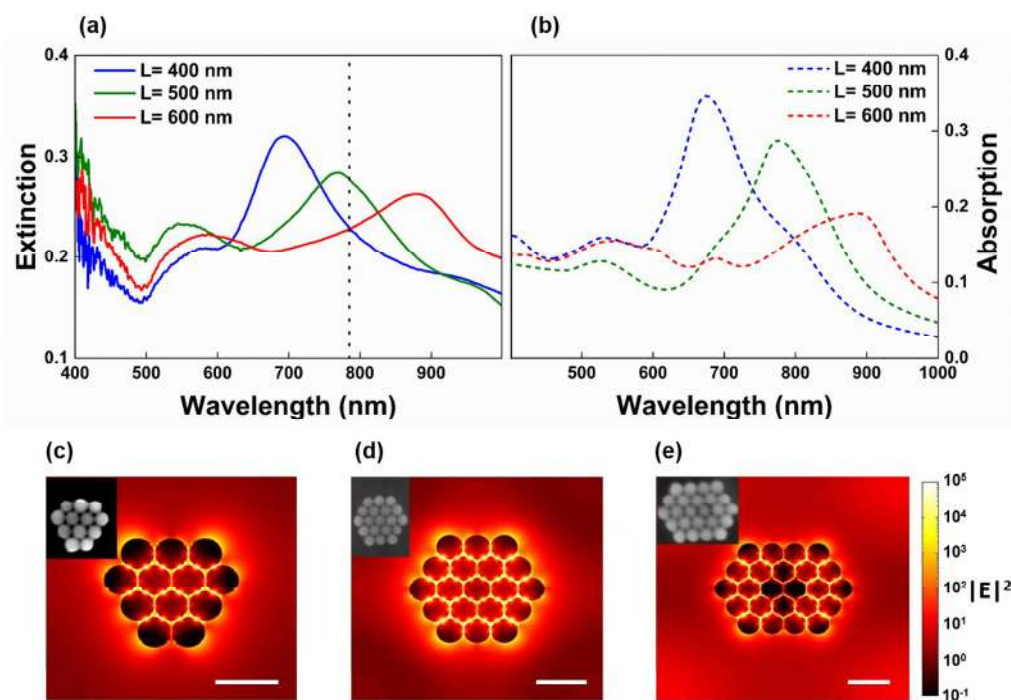


**Figure 4.** (a) Extinction spectra measured from AuNS arrays for varying lattice parameter  $L$ . The black dashed line marks the excitation laser wavelength used for surface-enhanced Raman spectroscopy,  $\lambda=785$  nm. (b) Absorption spectra from FDTD simulations. (c,d,e) Snapshots of a transversal cut of an AuNS superlattice unit cluster (insets are SEM micrographs with analogous configuration), showing the intensity of the electric field  $|E|^2$ , for lattice parameters  $L=400$  nm, 500 nm, and 600 nm, calculated at an excitation wavelength of 785 nm. Scale bars represent 100 nm.

Further insight into the physical origin of the hybridized lattice resonances is gained by comparing the measured extinction spectra with the simulated absorption of the

1  
2  
3 corresponding periodic structures, calculated by Finite Difference Time Domain  
4 simulations (FDTD). This comparison is displayed in **Figure 4a,b** for assemblies with  
5  $L=400, 500,$  and  $600$  nm, all having similar filling factors of AuNS ( $FF=0.25 - 0.27$ ),  
6 which correspond to maximum particle densities of 75, 76 and 83 AuNS/ $\mu\text{m}^2$ ,  
7 respectively. The values of AuNSs per unit area were calculated by inspection of SEM  
8 micrographs (**Table S1**). Corresponding SEM images of each model cluster type, with  
9 similar nanoparticle density, are included as insets in **Figure 4c,d,e**. As exemplified in  
10 the Supporting Information (**Figure S3**), the cluster size was found to influence the  
11 position of the optical resonance only marginally, for assemblies containing 9 or more  
12 particles. Still, variations in the configuration and orientation of the clusters lead to a  
13 slight damping of the extinction intensity and an increase of the full-width-at-half-  
14 maximum (FWHM) in the experimental data, as compared to numerical simulations of  
15 periodically arranged, identical clusters. Aside from that, we find excellent agreement  
16 between the measured and the calculated spectra.  
17  
18  
19  
20  
21  
22  
23  
24  
25  
26  
27  
28  
29  
30  
31  
32  
33

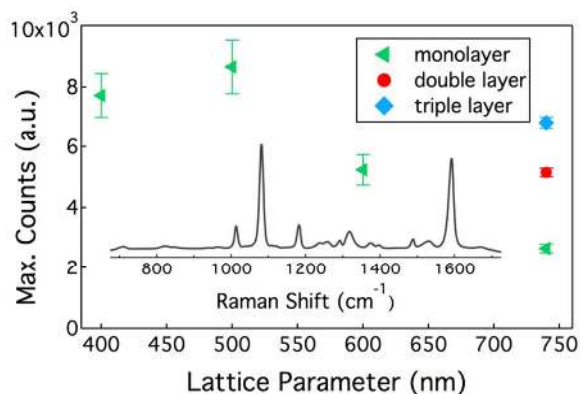
34 In general, the spectral position of the plasmon resonances is expected to correlate with  
35 the excitation of the highest local field factor and to affect the maximum Raman signal  
36 enhancement.<sup>8</sup> This should allow us to engineer the optical properties of the AuNS  
37 assemblies in a straightforward manner, toward targeting excitation with a specific laser  
38 line. Herein, we focus on irradiation with a laser of 785 nm wavelength, which is often  
39 preferred for optical investigations of biological samples as it matches the first optical  
40 transparency window. Comparing the extinction spectra of supercrystal films with  
41 different geometries (**Figure 4a,b**), we find that arrays with lattice parameter  $L=500$  nm  
42 have their main resonance band close to 785 nm. Snapshots of the electric field intensity  
43  $|E|^2$  at a transversal section of the periodic AuNS cluster arrays (**Figure 4c-e**) also  
44 display the highest enhancement for the lattice with  $L=500$  nm, under excitation at 785  
45  
46  
47  
48  
49  
50  
51  
52  
53  
54  
55  
56  
57  
58  
59  
60

1  
2  
3 nm. This extra field enhancement originates from the periodic arrangement of the  
4  
5 plasmonic clusters in a square lattice, which becomes obvious when comparing the field  
6  
7 enhancement profiles of isolated and periodically arranged clusters (**Figure S5, SI**).  
8  
9 Average enhancement factor spectra, calculated (see **Methods**) by averaging the surface  
10  
11 integral of the field enhancement factor  $\frac{|E|^4}{|E_0|^4}$  over the whole surface of the available  
12  
13 gold nanospheres, where  $E_0$  is the incident electric field, further corroborate the lattice-  
14  
15 dependent enhancement effect and again predict the strongest fields for  $L= 500$  nm  
16  
17 (**Figure S6, SI**).<sup>44</sup>  
18  
19

20  
21 To verify this analysis experimentally, we further investigated the performance of  
22  
23 different cluster arrays as SERS substrates under 785 nm excitation, using 4-  
24  
25 acetamidothiophenol (4-AMTP) as a model probe. A representative SERS spectrum of  
26  
27 4-AMTP is shown as an inset in **Figure 5**, revealing the characteristic main vibrational  
28  
29 modes at 1081  $\text{cm}^{-1}$  (C-S and ring stretch) and at 1591  $\text{cm}^{-1}$  (ring stretch).<sup>45</sup> In order to  
30  
31 assess to what extent the lattice resonance mode influences the SERS signal of the  
32  
33 substrates, we compared different monolayered cluster arrays with  $L = 400, 500, 600,$   
34  
35 and 740 nm. Whereas the lattice resonances of the largest arrays are far away from the  
36  
37 spectral region of interest, we observed that for this geometry, clusters with up to three  
38  
39 AuNS layers can be obtained due to the increased depth of the holes in the mold  
40  
41 (**Figure S7**), which allowed us to study also the influence of cluster height on the SERS  
42  
43 enhancement.  
44  
45  
46

47  
48 We explored the local homogeneity of the samples, by recording 100 individual data  
49  
50 points over an area of  $10 \times 10 \mu\text{m}^2$  and averaging for each measurement. As the SERS  
51  
52 effect directly mirrors the near-field generated at the nanometer scale, even subtle  
53  
54 changes in the local NP order, as well as the number and geometry of hot spots, can  
55  
56  
57  
58  
59  
60

1  
2  
3 cause significant intensity fluctuations. Additionally, the 3D packing of AuNS into  
4  
5 multilayered structures is known to affect the SERS response.<sup>27</sup> Therefore, a precise  
6  
7 correlation of the local array morphology with the recorded signal enhancement was  
8  
9 ensured through SEM characterization of the sites selected for SERS measurements.  
10  
11 The results are summarized in **Figure 5**, where the baseline-corrected average intensity  
12  
13 of the 1081  $\text{cm}^{-1}$  vibration is plotted as a function of the lattice parameter, for a typical  
14  
15 set of measurements. For superlattices consisting of monolayer clusters (green  
16  
17 triangles), a decrease of  $L$  from 740 to 500 nm leads to a nearly linear signal increase by  
18  
19 over 200%, followed by a slight drop at  $L=400$  nm, in agreement with the predictions  
20  
21 from FDTD simulations. The sample with  $L=740$  nm further exemplifies how the  
22  
23 extension from 2D to 3D assembly affects the SERS response: with the transition from  
24  
25 monolayer to double layer clusters (red circle) the average SERS signal rises by more  
26  
27 than 90%, whereas a third layer (blue square) leads to a further signal enhancement of  
28  
29 only 30%. We attribute the higher counts to an increased hot spot density due to the 3D  
30  
31 packing. A detailed characterization of the probed arrays, as well as a plot of the SERS  
32  
33 intensity normalized by the surface density of particles, is provided in the Supporting  
34  
35 Information (**Figure S8, SI**).  
36  
37  
38  
39



40  
41  
42  
43  
44  
45  
46  
47  
48  
49  
50  
51  
52  
53  
54 **Figure 5.** SERS signal at  $1081 \text{ cm}^{-1}$ , as a function of the lattice parameter. The  
55 maximum SERS intensity was found for  $L=500$  nm, in agreement with the good spectral  
56  
57  
58  
59  
60

1  
2  
3 match between the lattice plasmon wavelength and the 785 nm excitation laser, whereas  
4 the resonances of arrays with shorter and longer lattice parameters are detuned from the  
5 excitation laser (see **Figure 4**). The error bars depict the standard deviation of the signal  
6 in the probed  $10 \times 10 \mu\text{m}^2$  areas. The inset spectrum was recorded on a sample with  $L =$   
7 500 nm.  
8  
9

10  
11  
12 Overall, samples with an optical resonance close to the excitation wavelength of the  
13 laser exhibited significantly higher SERS enhancement than detuned samples.  
14 Intriguingly, monolayer samples tailored to the excitation wavelength ( $L = 500$  nm)  
15 yielded a total signal, even higher than that from non-optimized multilayer arrays  
16 containing nearly three times as many particles ( $L = 740$  nm). It should be noted that for  
17 arrays with small lattice parameters the average local SERS signals typically fluctuated  
18 more (10-20% standard deviation for  $L = 400$  and 500 nm) than for assemblies with large  
19 lattice parameters (2-5% standard deviation for  $L = 600$  and 740 nm). Interestingly,  
20 probing monolayer arrays of varying quality with the same lattice parameter ( $L = 500$   
21 nm), revealed a clear correlation between the standard deviation and the average SERS  
22 signal. An example is displayed in **Figure 6a**, showing that ordered arrays (stdev~10%)  
23 reached up to 5 times higher enhancement than irregular ones (stdev~35%). SEM  
24 inspection further confirmed that both homogeneity and signal intensity are strongly  
25 correlated to the average cluster size, for a given  $L$ . Plotting the normalized signal at  
26  $1081 \text{ cm}^{-1}$  as a function of the average cluster size revealed that the pronounced increase  
27 in SERS enhancement is not exclusively due to an increased number of hot spots. As  
28 can be seen in **Figure 6b**, the counts per particle (*i.e.*, per hot spot) remained nearly  
29 constant below a threshold value of 15, above which further enhancement was  
30 registered until reaching the geometrically determined maximum cluster size of 19  
31 particles. The signal per particle achieved with full cluster arrays (*i.e.*, 19 particles for  
32  $L = 500$  nm) was at least 3 times higher than that for a random sub-monolayer, obtained  
33  
34  
35  
36  
37  
38  
39  
40  
41  
42  
43  
44  
45  
46  
47  
48  
49  
50  
51  
52  
53  
54  
55  
56  
57  
58  
59  
60

using the same method but a non-structured stamp. These observations are in agreement with FDTD simulations of different cluster arrays with  $L=500$  nm, predicting both a cluster size-dependent hybridization efficiency (**Figure S3**) and stronger near-field enhancement in periodic arrays, as compared to isolated clusters (**Figure S5, SI**). A certain scatter of the counts per particle observed for clusters of identical size can be attributed to local structural defects: as illustrated in **Figure 6c**, comparing two arrays with identical lattice parameter and average cluster diameter, the enhancement clearly depends on the degree of order within the assembly, *i.e.*, on the strength of the lattice resonance. Additional information on the homogeneity and reproducibility of the films is provided in the Supporting Information (Section 10).

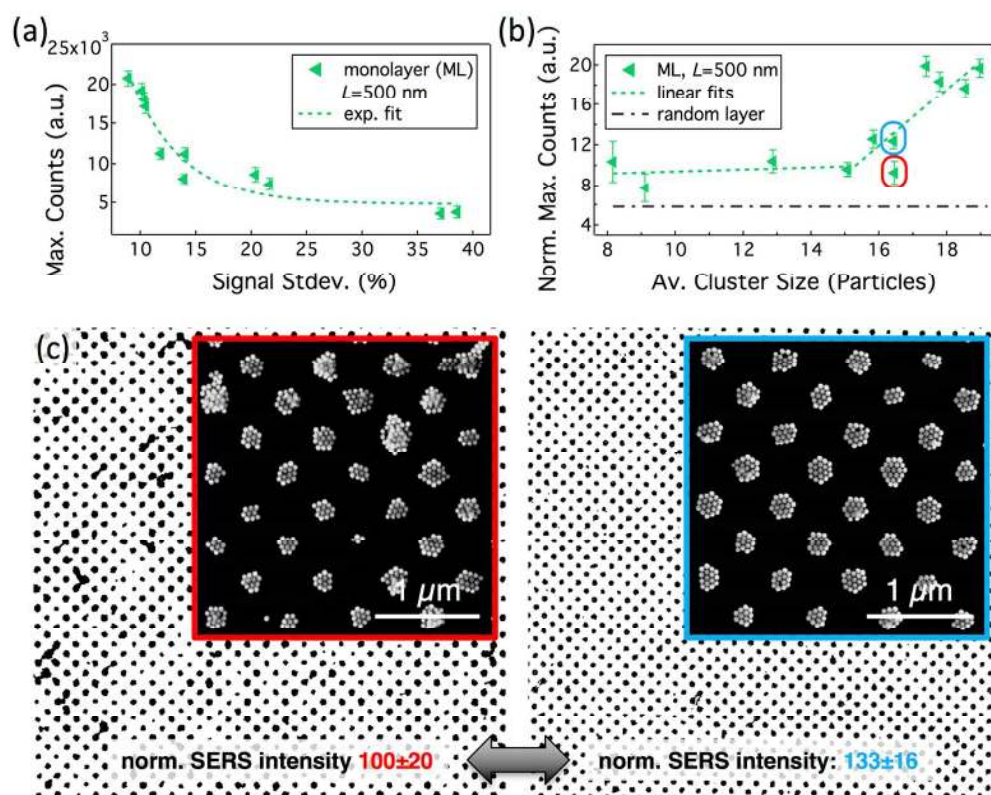


**Figure 6.** Correlated SERS and SEM characterization of monolayer arrays with fixed  $L=500$  nm and varying degree of assembly quality. (a) Increasing inhomogeneity, represented by the standard deviation (Stdev) of counts at  $1081\text{ cm}^{-1}$ , was accompanied by an overall decrease in signal strength. (b) The signal per particle was nearly constant for clusters smaller than 15 particles, but increased for larger clusters. The grey, dashed

1  
2  
3 line depicts the signal of a random monolayer (see **Figures S8,S9** for details). (c) For  
4 clusters of identical average diameter (marked by red and blue circles in b), the  
5 normalized signal depends strongly on the order within the array, illustrated with binary  
6 and inset grayscale SEM images. The error bars in (a,b) correspond to the standard  
7 deviation of the signal within the probed  $10 \times 10 \mu\text{m}^2$  areas.  
8  
9

## 10 11 **Conclusions**

12  
13  
14 We have demonstrated the organization of gold nanospheres into square array  
15 supercrystals with different lattice parameters, from 400 to 1600 nm, by using patterned  
16 PDMS molds as templates. The obtained 2D supercrystals exhibited well-defined  
17 resonance bands in the extinction spectra, which were tunable throughout the visible  
18 and NIR ranges, as a function of the lattice parameter, and were accurately reproduced  
19 by FDTD simulations. Theoretical modeling confirmed that the resonances originate  
20 from the hybridization of photonic lattice modes with plasmonic resonances sustained  
21 by individual AuNP clusters. The presence of such lattice plasmons guided the  
22 fabrication of supercrystal films with resonances targeting specific laser lines. We  
23 additionally explored the performance of 2D cluster arrays as SERS substrates, using 4-  
24 AMTP as a model Raman probe. Correlation of Raman and SEM measurements  
25 demonstrated that, lattices with a periodicity  $L=500$  nm were the most effective SERS  
26 platforms under 785 nm laser excitation, in agreement with the predictions by a simple  
27 model based on extinction. The signal intensity was also found to strongly depend on  
28 the degree of order within the arrays, and, intriguingly, monolayer clusters with the  
29 optimal lattice parameter may even display larger enhancement than non-optimized  
30 multilayered assemblies. Investigation of  $L=500$  nm monolayer arrays of different  
31 qualities indicated that the SERS intensity per particle grows linearly with the particle  
32 number, for clusters containing more than 15 particles, eventually reaching over three-  
33  
34  
35  
36  
37  
38  
39  
40  
41  
42  
43  
44  
45  
46  
47  
48  
49  
50  
51  
52  
53  
54  
55  
56  
57  
58  
59  
60



1  
2  
3 fold enhancement as compared to non-resonant random assemblies. This process thus  
4  
5 leads the way toward highly efficient, uniform and reproducible SERS substrates.  
6

## 7 8 **Methods**

9  
10 **Materials.** Hexadecyltrimethylammonium chloride (CTAC, 25% W/W), hydrogen  
11  
12 tetrachloroaurate trihydrate ( $\text{HAuCl}_4 \cdot 3\text{H}_2\text{O}$ ,  $\geq 99.9\%$ ), L-ascorbic acid ( $\geq 99\%$ ), sodium  
13  
14 hypochlorite solution (10-15% available chlorine), sodium borohydride ( $\text{NaBH}_4$ , 99%),  
15  
16 poly(ethylene glycol) methyl ether thiol (PEG-6K-SH,  $M_n = 6,000$  g/mol), and 4-  
17  
18 acetamidothiophenol were purchased from Sigma-Aldrich and employed without  
19  
20 further purification. Polydimethylsiloxane (Sylgard<sup>®</sup> 184) was bought from Dow  
21  
22 Corning. Water purified with a Milli-Q<sup>®</sup> system was used in all experiments.  
23  
24  
25

26 **Nanoparticles synthesis.** Monodisperse spherical gold nanoparticles with an average  
27  
28 diameter of 52 nm (standard deviation: 2 nm) were synthesized and characterized as  
29  
30 previously published.<sup>37</sup> In brief, a protocol that combines seeded growth with controlled  
31  
32 particle etching was used. Initial seeds were prepared by adding 50  $\mu\text{L}$  of a 0.05 M  
33  
34  $\text{HAuCl}_4$  solution to 5 mL of a 100 mM CTAC solution and injecting 200  $\mu\text{L}$  of a fresh  
35  
36  $\text{NaBH}_4$  (20 mM) solution while stirring vigorously. The resulting colloidal suspension  
37  
38 was diluted by a factor of 10 with 100 mM CTAC solution. These initial seeds were  
39  
40 grown to 10 nm diameter by mixing 900  $\mu\text{L}$  of the diluted gold colloid with 10 mL of  
41  
42 25 mM CTAC solution and 40  $\mu\text{L}$  of 100 mM ascorbic acid, followed by injection of 50  
43  
44  $\mu\text{L}$  of a 50 mM  $\text{HAuCl}_4$  solution under rapid stirring. Growth to the final size was  
45  
46 achieved by diluting 250  $\mu\text{L}$  of the obtained suspension with 100 mL of a 25 mM  
47  
48 CTAC solution, adding 400  $\mu\text{L}$  of 100 mM ascorbic acid, and injecting 500  $\mu\text{L}$  of a 50  
49  
50 mM  $\text{HAuCl}_4$  solution under rapid stirring. After 1 h, 100  $\mu\text{L}$  of a dilute sodium  
51  
52 hypochlorite solution (1-1.5 wt% of available chlorine) were added stirring vigorously.  
53  
54  
55  
56  
57  
58  
59  
60

1  
2  
3 After 5 min, 25  $\mu$ L of a 50 mM HAuCl<sub>4</sub> solution were added and the reaction was left at  
4  
5 30 °C until a constant absorption at 400 nm (Abs<sub>400</sub>) was reached. The particles were  
6  
7 then cleaned immediately by centrifuge washing twice at 3500 rpm with 2 mM CTAC  
8  
9 solution. PEGylation was typically done by setting the particles up to an Au<sup>0</sup>  
10  
11 concentration of 10 mM (according to Abs<sub>400</sub>,<sup>46,47</sup>) in 1 mM CTAC solution and adding  
12  
13 1 mg of solid PEG-6k-SH per mL dispersion. The ligand exchange took place overnight  
14  
15 and was followed by centrifuge washing with 300  $\mu$ M CTAC three times. Thereby, the  
16  
17 particle concentration was increased up to 800 mM to create a stock dispersion.  
18  
19

20  
21 **Nanoparticle assembly.** For templated assembly, aliquots of the stock dispersion were  
22  
23 diluted with suitable CTAC solutions to reach a final surfactant concentration of 50  $\mu$ M  
24  
25 and Au<sup>0</sup> concentrations between 13 and 90 mM, as denoted in the text. Borosilicate  
26  
27 microscope coverslips (Menzel<sup>TM</sup>, #1.5) cut into pieces of 8 x 4 mm<sup>2</sup> or 12 x 12 mm<sup>2</sup>  
28  
29 were used as substrates, depending on the size of the PDMS mold. The substrate  
30  
31 preparation protocol comprised cleaning with Hellmanex<sup>TM</sup> III solution, sonication in  
32  
33 isopropanol, rinsing with water, and subsequent hydrophilization in a UV-O<sub>3</sub> chamber  
34  
35 (ProCleaner<sup>TM</sup>) for at least 45 min. To fabricate periodically arranged plasmonic  
36  
37 supercrystals, 1  $\mu$ L droplets of PEGylated AuNS dispersion were placed onto structured  
38  
39 soft PDMS molds and covered with a hydrophilized glass substrate. After drying, the  
40  
41 substrates were removed and the PDMS molds cleaned for reuse with adhesive tape,  
42  
43 followed by rinsing with ethanol and water.  
44  
45  
46  
47  
48  
49

50  
51 **Soft molds fabrication.** Soft PDMS molds were fabricated by pouring a 10:1 mixture  
52  
53 of prepolymer and curing agent onto patterned silicon masters or their negative replicas  
54  
55 with OrmoStamp® (Microresist Technology).<sup>48,49</sup> The mixtures were degassed for 2  
56  
57  
58  
59  
60

1  
2  
3 hours to increase the percolation of the polymer inside the nanostructures and then  
4  
5 cured for 45 min at 100 °C. The PDMS molds were characterized by atomic force  
6  
7 microscopy (see **Figure S7, SI**).  
8  
9

10 **UV-vis measurements.** Extinction spectra of dispersed AuNSs were recorded with an  
11  
12 Agilent 8453 UV-vis spectrophotometer, using polystyrene cuvettes.  
13  
14

15 **FTIR measurements.** An FTIR spectrometer (Vertex 70 Bruker) attached to an optical  
16  
17 microscope (Hyperion, Bruker) was used for far-field reflection and transmission  
18  
19 measurements in the 400 to 3000 nm range. The background reflection spectrum was  
20  
21 set with a silver mirror with 96% reflectivity in the tested range of wavelengths and the  
22  
23 transmission background without sample. Both reflection and transmission spectra were  
24  
25 collected with a 4X objective with a numerical aperture (N.A.) of 0.10 and a spatial  
26  
27 mask. The spot size was fixed at 600 x 600  $\mu\text{m}^2$ .  
28  
29  
30

31 **Scanning electron microscopy.** SEM images were recorded without prior sputtering  
32  
33 using a FEI Quanta 250 microscope operated in low vacuum mode with an acceleration  
34  
35 voltage of 10 kV and a working distance of 5 mm. The local particle densities were  
36  
37 evaluated after suitable contrast and bright adjustments using the particle counting  
38  
39 functionality of ImageJ. The arrays were categorized, either by manually counting the  
40  
41 number of layered clusters or, where applicable, by comparing the cluster count and  
42  
43 occupied area in overexposed (yields bottom layer) and underexposed (yields top layer)  
44  
45 images. Thereby, structures with more than 1 particle sitting on top of a 2D cluster were  
46  
47 registered as layered, and regions with less than 30% double layer content were defined  
48  
49 as monolayer arrays.  
50  
51  
52  
53  
54  
55  
56  
57  
58  
59  
60

1  
2  
3 **Transmission electron microscopy.** TEM images were recorded with a JEOL JEM-  
4 1400PLUS at an acceleration voltage of 120 kV. The particles were deposited from  
5 dilute dispersion on carbon-coated 400 square mesh copper TEM grids.  
6  
7

8  
9  
10 **Numerical simulations.** Numerical calculations were performed using Lumerical  
11 FDTD solutions ([www.lumerical.com](http://www.lumerical.com)). The structural parameters of AuNS clusters for  
12 modelling were set according to the size measured from TEM images with an  
13 interparticle distance of 1 nm. The dispersion model of gold was taken from Johnson  
14 and Christy<sup>50</sup> and the glass substrate was considered a medium with dispersive  
15 refractive index around  $n_{glass} \sim 1.54 - 1.51$  at 400 nm and 1000 nm, respectively. An  
16 unpolarized plane wave source impinging at normal incidence to different periodic  
17 AuNS clusters was modelled with a wavelength ranging from 400 nm to 2000 nm,  
18 providing a good agreement with experimental results. A nonuniform FDTD mesh  
19 method was adapted to save computation resources and calculation time. Enhancement  
20 factors have been calculated measuring the surface integral of the electric field  
21 enhancement on the surface of the gold nanospheres and normalized by the total number  
22 of particles per  $\mu\text{m}^2$ .  
23  
24  
25  
26  
27  
28  
29  
30  
31  
32  
33  
34  
35  
36  
37  
38

$$\frac{\iint \frac{|E|^4}{|E_0|^4} dS}{\iint dS} \quad (1)$$

39  
40  
41  
42  
43

44 **Surface-enhanced Raman scattering (SERS) spectroscopy.** An optimized cleaning  
45 procedure was necessary prior to the SERS measurements. To this end, the nanoparticle  
46 assemblies were treated first with oxygen plasma (Diener PICO, 0.4 mbar O<sub>2</sub>, 200 W, 1  
47 min) and then exposed to UV-O<sub>3</sub> treatment for 30 min. Immediately after cleaning, the  
48 substrates were incubated in 800  $\mu\text{L}$  of a freshly prepared 0.1 mM aqueous 4-AMTP  
49 solution for at least 60 min. Next, the samples were intensively rinsed with water to  
50  
51  
52  
53  
54  
55  
56  
57  
58  
59  
60

1  
2  
3 remove unbound molecules and dried in a N<sub>2</sub> stream. SERS measurements were carried  
4  
5 out in a confocal Raman microscope (inVia™ Reflex, Renishaw) equipped with a 785  
6  
7 nm diode laser (nominal output 300 mW) as excitation source, 1200 grooves/mm  
8  
9 diffraction grating and a front-illuminated Peltier-cooled CCD camera (1024 pixel x 512  
10  
11 pixel). SERS spectra were measured using a 100x objective with an N.A. of 0.9, a laser  
12  
13 power of 1.7 mW (at the surface), and an integration time of 1 s. For data analysis, 100  
14  
15 spectra were taken from 10 x 10 μm<sup>2</sup> areas with a distance of 1 μm (in x and y) between  
16  
17 each point and averaged afterwards. To check the homogeneity of the assemblies the  
18  
19 measurements were repeated at least at three positions spaced at mm intervals and  
20  
21 randomly distributed over the substrate for each sample. In the same manner, the batch-  
22  
23 to-batch reproducibility was also probed for at least two sample batches of each lattice  
24  
25 parameter. For lattice parameter-dependent SERS plots, the averaged 1081 cm<sup>-1</sup> signals  
26  
27 were fitted and the intensities plotted after baseline subtraction using the WIRE™ 4  
28  
29 software package.  
30  
31  
32  
33  
34  
35

36  
37 *Acknowledgements.* The authors thank Dr. Guillermo González-Rubio for providing  
38  
39 nanoparticles and assistance with the synthesis. C.H. acknowledges funding from the  
40  
41 Alexander von Humboldt Foundation through a Feodor Lynen fellowship. Funding by  
42  
43 the Spanish Ministerio de Economía, Industria y Competitividad (MINECO) is  
44  
45 gratefully acknowledged (Grant SEV-2015-0496 in the framework of the Spanish  
46  
47 Severo Ochoa Centre of Excellence program, and Grants MAT2016-79053-P and  
48  
49 MAT2017-86659-R). A.M. is grateful to the funding from the European Research  
50  
51 Council (ERC) under the European Union's Horizon 2020 research and innovation  
52  
53 program (grant agreement No. 637116, ENLIGHTMENT).  
54  
55  
56  
57  
58  
59  
60

1  
2  
3  
4  
5 *Supporting Information Available.* Supporting Information is available online free of  
6  
7 charge: Further insight on the optimization of nanoparticle assembly including  
8  
9 structural characterization of the PDMS mold; details of the theoretical calculations  
10  
11 (near field intensity, enhancement factor, Rayleigh anomalies); details on SERS  
12  
13 measurements and calculation of normalized signal intensity per particle and random  
14  
15 layer characterization.  
16  
17  
18  
19  
20  
21  
22  
23  
24  
25  
26  
27  
28  
29  
30  
31  
32  
33  
34  
35  
36  
37  
38  
39  
40  
41  
42  
43  
44  
45  
46  
47  
48  
49  
50  
51  
52  
53  
54  
55  
56  
57  
58  
59  
60

## References

- (1) Fedick, P. W.; Bills, B. J.; Manicke, N. E.; Cooks, R. G. Forensic Sampling and Analysis from a Single Substrate: Surface-Enhanced Raman Spectroscopy Followed by Paper Spray Mass Spectrometry. *Anal. Chem.* **2017**, *89*, 10973–10979.
- (2) Baumberg, J.; Bell, S.; Bonifacio, A.; Chikkaraddy, R.; Chisanga, M.; Corsetti, S.; Delfino, I.; Eremina, O.; Fasolato, C.; Faulds, K.; Fleming, H.; Goodacre, R.; Graham, D.; Hardy, M.; Jamieson, L.; Keyes, T.; Królikowska, A.; Kuttner, C.; Langer, J.; et al. SERS in Biology/biomedical SERS: General Discussion. *Faraday Discuss.* **2017**, *205*, 429–456.
- (3) Premasiri, W. R.; Chen, Y.; Fore, J.; Brodeur, A.; Ziegler, L. D. SERS Biomedical Applications: Diagnostics, Forensics, and Metabolomics. *Front. Adv. Mol. Spectrosc.* **2017**, 327–367.
- (4) Sun, F.; Hung, H.-C.; Sinclair, A.; Zhang, P.; Bai, T.; Galvan, D. D.; Jain, P.; Li, B.; Jiang, S.; Yu, Q. Hierarchical Zwitterionic Modification of a SERS Substrate Enables Real-Time Drug Monitoring in Blood Plasma. *Nat. Commun.* **2016**, *7*, 13437.
- (5) Graham, D.; Goodacre, R.; Arnolds, H.; Masson, J.-F.; Schatz, G.; Baumberg, J.; Kim, D.-H.; Aizpurua, J.; Lum, W.; Silvestri, A.; de Nijs, B.; Xu, Y.; Di Martino, G.; Natan, M.; Schlücker, S.; Wuytens, P.; Bruzas, I.; Kuttner, C.; Hardy, M.; et al. Theory of SERS Enhancement: General Discussion. *Faraday Discuss.* **2017**, *205*, 173–211.
- (6) Jeanmaire, D. L.; Van Duyne, R. P. Surface Raman Spectroelectrochemistry: Part I. Heterocyclic, Aromatic, and Aliphatic Amines Adsorbed on the Anodized Silver Electrode. *J. Electroanal. Chem. Interfacial Electrochem.* **1977**, *84*, 1–20.
- (7) Albrecht, M. G.; Creighton, J. A. Anomalously Intense Raman Spectra of Pyridine at a Silver Electrode. *J. Am. Chem. Soc.* **1977**, *99*, 5215–5217.
- (8) Moskovits, M. Persistent Misconceptions Regarding SERS. *Phys. Chem. Chem. Phys.* **2013**, *15*, 5301–5311.
- (9) Jahn, M.; Patze, S.; Hidi, I. J.; Knipper, R.; Radu, A. I.; Mühlig, A.; Yüksel, S.; Peksa, V.; Weber, K.; Mayerhöfer, T.; Cialla-May, D.; Popp, J. Plasmonic Nanostructures for Surface Enhanced Spectroscopic Methods. *Analyst* **2016**, *141*, 756–793.
- (10) Di Martino, G.; Turek, V. A.; Tserkezis, C.; Lombardi, A.; Kuhn, A.; Baumberg, J. J. Plasmonic Response and SERS Modulation in Electrochemical Applied Potentials. *Faraday Discuss.* **2017**, *205*, 537–545.
- (11) Luo, S.-C.; Sivashanmugan, K.; Liao, J.-D.; Yao, C.-K.; Peng, H.-C. Nanofabricated SERS-Active Substrates for Single-Molecule to Virus Detection *in Vitro*: A Review. *Biosens. Bioelectron.* **2014**, *61*, 232–240.
- (12) Willets, K. A.; Van Duyne, R. P. Localized Surface Plasmon Resonance Spectroscopy and Sensing. *Annu. Rev. Phys. Chem.* **2007**, *58*, 267–297.

- 1  
2  
3 (13) Yang, A.; Hoang, T. B.; Dridi, M.; Deeb, C.; Mikkelsen, M. H.; Schatz, G. C.;  
4 Odom, T. W. Real-Time Tunable Lasing from Plasmonic Nanocavity Arrays.  
5 *Nat. Commun.* **2015**, *6*.
- 6  
7 (14) Cha, H.; Yoon, J. H.; Yoon, S. Probing Quantum Plasmon Coupling Using Gold  
8 Nanoparticle Dimers with Tunable Interparticle Distances Down to the  
9 Subnanometer Range. *ACS Nano* **2014**, *8*, 8554–8563.
- 10  
11 (15) Hao, E.; Schatz, G. C. Electromagnetic Fields around Silver Nanoparticles and  
12 Dimers Shape Effects in Plasmon Resonance of Individual Colloidal Silver  
13 Nanoparticles Experimental Observation of Narrow Surface Plasmon Resonances  
14 in Gold Nanoparticle Arrays Electromagnetic Fields. *J. Chem. Phys.* **2004**, *120*,  
15 11101–10871.
- 16  
17 (16) Huang, Y.; Zhou, Q.; Hou, M.; Ma, L.; Zhang, Z. Nanogap Effects on near-and  
18 Far-Field Plasmonic Behaviors of Metallic Nanoparticle Dimers. *Phys. Chem.*  
19 *Chem. Phys.* **2015**, *17*, 29293–29298.
- 20  
21 (17) Mosier-Boss, P. A. Review of SERS Substrates for Chemical Sensing.  
22 *Nanomaterials* **2017**, *7*, 142 (1-30).
- 23  
24 (18) Strobbia, P.; Languirand, E.; Cullum, B. M. Recent Advances in Plasmonic  
25 Nanostructures for Sensing: A Review. *Opt. Eng.* **2015**, *54*, 100902.
- 26  
27 (19) Kraus, T.; Malaquin, L.; Schmid, H.; Riess, W.; Spencer, N. D.; Wolf, H.  
28 Nanoparticle Printing with Single-Particle Resolution. *Nat. Nanotechnol.* **2007**, *2*,  
29 570–576.
- 30  
31 (20) Hanske, C.; Müller, M. B.; Bieber, V.; Tebbe, M.; Jessl, S.; Wittemann, A.; Fery,  
32 A. The Role of Substrate Wettability in Nanoparticle Transfer from Wrinkled  
33 Elastomers: Fundamentals and Application toward Hierarchical Patterning.  
34 *Langmuir* **2012**, *28*, 16745–16750.
- 35  
36 (21) Volk, K.; Fitzgerald, J. P. S.; Ruckdeschel, P.; Retsch, M.; König, T. A. F.; Karg,  
37 M. Reversible Tuning of Visible Wavelength Surface Lattice Resonances in Self-  
38 Assembled Hybrid Monolayers. *Adv. Opt. Mater.* **2017**, *5*, 1600971.
- 39  
40 (22) Greybush, N. J.; Liberal, I.; Malassis, L.; Kikkawa, J. M.; Engheta, N.; Murray,  
41 C. B.; Kagan, C. R. Plasmon Resonances in Self-Assembled Two-Dimensional  
42 Au Nanocrystal Metamolecules. *ACS Nano* **2017**, *11*, 2917–2927.
- 43  
44 (23) Gu, X.; Tian, S.; Zhou, Q.; Adkins, J.; Gu, Z.; Li, X.; Zheng, J. SERS Detection  
45 of Polycyclic Aromatic Hydrocarbons on a Bowl-Shaped Silver Cavity Substrate.  
46 *RSC Adv.* **2013**, *3*, 25989.
- 47  
48 (24) Polavarapu, L.; Liz-Marzán, L. M. Towards Low-Cost Flexible Substrates for  
49 Nanoplasmonic Sensing. *Phys. Chem. Chem. Phys.* **2013**, *15*, 5288.
- 50  
51 (25) Bodelón, G.; Montes-García, V.; López-Puente, V.; Hill, E. H.; Hamon, C.;  
52 Sanz-Ortiz, M. N.; Rodal-Cedeira, S.; Costas, C.; Celiksoy, S.; Pérez-Juste, I.;  
53 Scarabelli, L.; La Porta, A.; Pérez-Juste, J.; Pastoriza-Santos, I.; Liz-Marzán, L.  
54 M. Detection and Imaging of Quorum Sensing in *Pseudomonas Aeruginosa*  
55 Biofilm Communities by Surface-Enhanced Resonance Raman Scattering. *Nat.*  
56 *Mater.* **2016**, *15*, 1203–1211.
- 57  
58  
59  
60



- 1  
2  
3 (26) Ross, M. B.; Mirkin, C. A.; Schatz, G. C. Optical Properties of One-, Two-, and  
4 Three-Dimensional Arrays of Plasmonic Nanostructures. *J. Phys. Chem. C* **2016**,  
5 *120*, 816–830.
- 6  
7 (27) Hamon, C.; Novikov, S. M.; Scarabelli, L.; Solís, D. M.; Altantzis, T.; Bals, S.;  
8 Taboada, J. M.; Obelleiro, F.; Liz-Marzán, L. M. Collective Plasmonic Properties  
9 in Few-Layer Gold Nanorod Supercrystals. *ACS Photonics* **2015**, *2*, 1482–1488.
- 10  
11 (28) Hanske, C.; Tebbe, M.; Kuttner, C.; Bieber, V.; Tsukruk, V. V.; Chanana, M.;  
12 König, T. A. F.; Fery, A. Strongly Coupled Plasmonic Modes on Macroscopic  
13 Areas via Template-Assisted Colloidal Self-Assembly. *Nano Lett.* **2014**, *14*,  
14 6863–6871.
- 15  
16 (29) Hentschel, M.; Dregely, D.; Vogelgesang, R.; Giessen, H.; Liu, N. Plasmonic  
17 Oligomers: The Role of Individual Particles in Collective Behavior. *ACS Nano*  
18 **2011**, *5*, 2042–2050.
- 19  
20 (30) Wang, D.; Yang, A.; Wang, W.; Hua, Y.; Schaller, R. D.; Schatz, G. C.; Odom,  
21 T. W. Band-Edge Engineering for Controlled Multi-Modal Nanolasing in  
22 Plasmonic Superlattices. *Nat. Nanotechnol.* **2017**, *12*, 889–894.
- 23  
24 (31) Yan, B.; Thubagere, A.; Premasiri, W. R.; Ziegler, L. D.; Negro, L. D.; Reinhard,  
25 B. M. Engineered SERS Substrates with Multiscale Signal Enhancement:  
26 Nanoparticle Cluster Arrays. *ACS Nano* **2009**, *3*, 1190–1202.
- 27  
28 (32) Yan, B.; Boriskina, S. V.; Reinhard, B. M. Design and Implementation of Noble  
29 Metal Nanoparticle Cluster Arrays for Plasmon Enhanced Biosensing. *J. Phys.*  
30 *Chem. C* **2011**, *115*, 24437–24453.
- 31  
32 (33) Wang, D.; Yang, A.; Hryn, A. J.; Schatz, G. C.; Odom, T. W. Superlattice  
33 Plasmons in Hierarchical Au Nanoparticle Arrays. *ACS Photonics* **2015**, *2*, 1789–  
34 1794.
- 35  
36 (34) Hamon, C.; Sanz-Ortiz, M. N.; Modin, E.; Hill, E. H.; Scarabelli, L.; Chuvilin,  
37 A.; Liz-Marzán, L. M. Hierarchical Organization and Molecular Diffusion in  
38 Gold Nanorod/silica Supercrystal Nanocomposites. *Nanoscale* **2016**, *8*, 7914–  
39 7922.
- 40  
41 (35) Hamon, C.; Novikov, S.; Scarabelli, L.; Basabe-Desmonts, L.; Liz-Marzán, L. M.  
42 Hierarchical Self-Assembly of Gold Nanoparticles into Patterned Plasmonic  
43 Nanostructures. *ACS Nano* **2014**, *8*, 10694–10703.
- 44  
45 (36) Macias, G.; Alba, M.; Marsal, L. F.; Mihi, A. Surface Roughness Boosts the  
46 SERS Performance of Imprinted Plasmonic Architectures. *J. Mater. Chem. C*  
47 **2016**, *4*, 3970–3975.
- 48  
49 (37) Hanske, C.; González-Rubio, G.; Hamon, C.; Formentín, P.; Modin, E.; Chuvilin,  
50 A.; Guerrero-Martínez, A.; Marsal, L. F.; Liz-Marzán, L. M. Large-Scale  
51 Plasmonic Pyramidal Supercrystals via Templated Self-Assembly of  
52 Monodisperse Gold Nanospheres. *J. Phys. Chem. C* **2017**, *121*, 10899–10906.
- 53  
54 (38) Yoon, J. H.; Selbach, F.; Langolf, L.; Schlücker, S. Ideal Dimers of Gold  
55 Nanospheres for Precision Plasmonics: Synthesis and Characterization at the  
56 Single-Particle Level for Identification of Higher Order Modes. *Small* **2018**, *14*,  
57

1  
2  
3 1702754.

- 4 (39) Bao, K.; Mirin, N. A.; Nordlander, P. Fano Resonances in Planar Silver  
5 Nanosphere Clusters. *Appl. Phys. A* **2010**, *100*, 333–339.
- 6 (40) Guo, R.; Hakala, T. K.; Törmä, P. Geometry Dependence of Surface Lattice  
7 Resonances in Plasmonic Nanoparticle Arrays. *Phys. Rev. B* **2017**, *95*, 155423.
- 8 (41) Khlopin, D.; Laux, F.; Wardley, W. P.; Martin, J.; Wurtz, G. A.; Plain, J.; Bonod,  
9 N.; Zayats, A. V.; Dickson, W.; Gérard, D. Lattice Modes and Plasmonic  
10 Linewidth Engineering in Gold and Aluminum Nanoparticle Arrays. *J. Opt. Soc.*  
11 *Am. B* **2017**, *34*, 691–700.
- 12 (42) Auguié, B.; Bendaña, X. M.; Barnes, W. L.; García de Abajo, F. J. Diffractive  
13 Arrays of Gold Nanoparticles near an Interface: Critical Role of the Substrate.  
14 *Phys. Rev. B* **2010**, *82*, 155447.
- 15 (43) Le Ru, E.; Etchegoin, P. Principles of Surface Enhanced Raman Spectroscopy  
16 and Related Plasmonic Effects. *Elsevier* **2009**.
- 17 (44) Huang, Y.; Zhang, X.; Ringe, E.; Hou, M.; Ma, L.; Zhang, Z. Tunable Lattice  
18 Coupling of Multipole Plasmon Modes and Near-Field Enhancement in Closely  
19 Spaced Gold Nanorod Arrays. *Sci. Rep.* **2016**, *6*, 23159.
- 20 (45) Zhang, Y.; Li, X.; Xue, B.; Kong, X.; Liu, X.; Tu, L.; Chang, Y. A Facile and  
21 General Route to Synthesize Silica-Coated SERS Tags with the Enhanced Signal  
22 Intensity. *Sci. Rep.* **2015**, *5*, 14934.
- 23 (46) Rodríguez-Lorenzo, L.; Álvarez-Puebla, R. A.; García de Abajo, F. J.; Liz-  
24 Marzán, L. M. Surface Enhanced Raman Scattering Using Star-Shaped Gold  
25 Colloidal Nanoparticles. *J. Phys. Chem. C* **2010**, *114*, 7336–7340.
- 26 (47) Scarabelli, L.; Sánchez-Iglesias, A.; Pérez-Juste, J.; Liz-Marzán, L. M. A “Tips  
27 and Tricks” Practical Guide to the Synthesis of Gold Nanorods. *J. Phys. Chem.*  
28 *Lett.* **2015**, *6*, 4270–4279.
- 29 (48) Xia, Y.; Rogers, J. A.; Paul, K. E.; Whitesides, G. M. Unconventional Methods  
30 for Fabricating and Patterning Nanostructures. *Chem. Rev.* **1999**, *99*, 1823–1848.
- 31 (49) Qin, D.; Xia, Y.; Whitesides, G. M. Soft Lithography for Micro- and Nanoscale  
32 Patterning. *Nat. Protoc.* **2010**, *5*, 491–502.
- 33 (50) Johnson, P. B.; Christy, R. W. Optical Constants of the Noble Metals. *Phys. Rev.*  
34 *B* **1972**, *6*, 4370–4379.
- 35  
36  
37  
38  
39  
40  
41  
42  
43  
44  
45  
46  
47  
48  
49  
50  
51  
52  
53  
54  
55  
56  
57  
58  
59  
60

1  
2  
3  
4  
5  
6  
7  
8  
9  
10  
11  
12  
13  
14  
15  
16  
17  
18

